Photodissociation of ClO

Marloes van Beek

August 31, 2011

Abstract

We have used the coupled channel method to better understand the photodissociation of ClO. Therefore we have calculated the spin-orbit coupling constants of the ten dissociative states that cross the $A^2\Pi$ state and also determined the linewidth and fine structure branching ratios [1]. These results have been compared with results of other calculations, including diabatic calculations and experiments. We have used three different sets of coupling constants and two different potentials of the $A^2\Pi$ state to produce the best agreement with the experiments. We have found that small differences in the potentials or shifting of the potentials have a large influence on the linewidth results and also the set of coupling constants are a big influence on both the linewidth and fine structure branching ratios. The best agreement with the experiments was produced using the coupling constants which are described in this report and the RKR potential by Howie *et al.*.

Chapter 1

Introduction

In 1991 Anderson *et al.* discovered that ClO is one of the molecules that are most responsible for the destruction of ozone. It is the biggest contributor of atomic Cl in the lower and middle stratosphere, which is very efficient in the destruction of ozone, via

$$O_3 + Cl \longrightarrow ClO + O_2,$$

$$ClO + O \longrightarrow Cl + O_2.$$

It is therefore important to have a detailed understanding of the chemistry of ClO, to model ozone concentrations in the atmosphere. The role of ClO is also important in photodissociation of $ClONO_2$ and Cl_2O, where ClO is a primary photofragment that may undergo secondary photolysis.

The diatom ClO consists of a chlorine and oxygen atom and is an open-shell molecule. The chlorine atom is a halogen and has 17 electrons, the oxygen atom has 8 electrons. The electronic configuration of the ClO ground state $X^2\Pi$ is $...(7\sigma)^2(2\pi)^4(3\pi^*)^3$. The molecule is excited from the ground state to the first excited state, the $A^2\Pi$ state, with electronic configuration $...(7\sigma)^2(2\pi)^3(3\pi^*)^4$ using UV light with $\lambda < 316$ nm.

There have been several experimental studies of the linewidth for different vibrations of the $A^2\Pi$ state. The most recent experiments were done using a cavity ring-down apparatus. Most studies focussed on $\Omega = 3/2$, but Howie *et al.* [2] also give some results for $\Omega = 1/2$.

The molecule dissociates through coupling by one of the ten repulsive potentials that cross the $A^2\Pi$ state, as shown in figure 1.1.

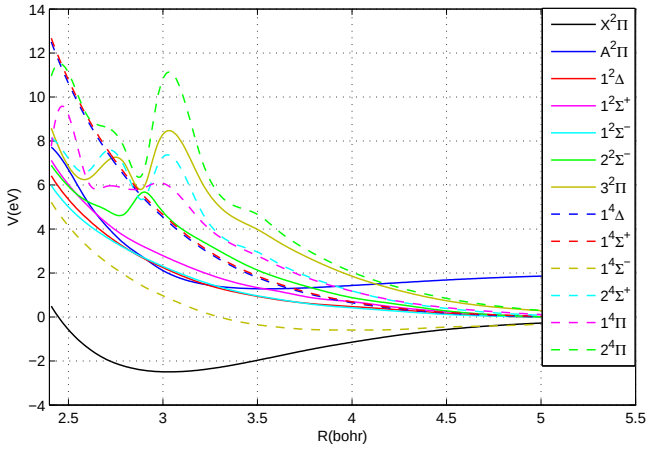

Figure 1.1: The *ab initio* potentials.

The potentials that were used are taken from Toniolo *et al.* [3]. For the $A^2\Pi$ state also a Rydberg-Klein-Rees (RKR) potential is available from Howie *et al.* [2].

From the excited $A^2\Pi$ state, there is a transition to an electronic repulsive state. The transition occurs through spin-orbit coupling or an avoided crossing. The $A^2\Pi$ state has the same symmetry as the $3^2\Pi$ state, therefore there is a mixing of the two wavefunctions to give an avoided crossing. The likeliness of the coupling with each state depends on the vibrational level of the excited state.

The electronic repulsive states decay into $O(^3P_J)$ and $Cl(^2P_J)$. For O $j_a = 0, 1, 2$ and Cl $j_b = \frac{1}{2}, \frac{3}{2}$. The combination of O and Cl depends on the repulsive state. The complete photodissociating process is descibed by:

$$ClO(X^2\Pi) \xrightarrow{h\nu} ClO(A^2\Pi) \longrightarrow Cl(^2P_j b) + O(^3P_j a).$$

The group of prof. North has done many experiments [4] on ClO to obtain the fine structure branching ratios. They have used an velocity-map ion-imaging apparatus. A pulsed molecular beam of ClO seeded in He and collimated by a conical skimmer was intersected at 90° by two co-propagating linearly polarized laser beams.

Lane *et al.* [5] have produced their own *ab initio* potentials and used them with their RKR potential to calculate the predissociation rates of the most promising repulsive state at $v' = 0 - 19$. Using these rates they computed the couplings to get the best fit of the linewidth with the experimental results. Kim *et al.* and Dooley *et al.* [1,4,6] have done experiments to determine the fine structure branching ratios of $v' = 0-11$ predissociation of the $A^2\Pi$ state. Kim *et al.* [6] have done some diabatic calculations to determine the theoretical fine structure branching ratios of $v' = 0 - 11$ and compared them to the experimental results.

The present work gives the results of *ab initio* calculations and compares them with the results of experiments [1, 2, 4, 6–8] and other theoretical works [3, 5, 6]. A part of this work has also been published together with experimental research [1].

The theory is described in Chapter 2 and the program used for the calculations in Chapter 3. Chapter 4 consists of the results and in Chapter 5 the conclusions are given.

Chapter 2

Theory

In the Fermi Golden Rule approximation the linewidth (full-width at half-maximum) Γ is given by [9]:

$$\Gamma(n,v) = \sum_{j_a j_b} \Gamma_{j_a j_b}(n,v) = \sum_{j_a j_b j_{ab} l M} \frac{2\pi}{\hbar} |\langle \psi_i(v) | V_{10} | \psi_{JM}^{(-) j_a j_b j_{ab} l} \rangle|^2, \tag{2.1}$$

where $\Gamma_{j_a j_b}(n,v)$ is the rate of decay into fine structure states $\mathrm{Cl}(^2\mathrm{P}_{j_a})$ $\mathrm{O}(^3\mathrm{P}_{j_b})$, ψ_i the $\mathrm{A}^2\Pi$ state, v the vibration quantumnumber of the $\mathrm{A}^2\Pi$ state, $\psi_{JM}^{(-) j_a j_b j_{ab} l}$ one of the dissociative states and V_{10} the coupling between the states. The lifetimes is related to the linewidth by:

$$\tau(n,v) = \frac{1}{\Gamma(n,v)}. \tag{2.2}$$

2.1 Branching Ratio

The correlated fine stucture branching ratios per dissociating state are defined as:

$$P_{j_a}(n,v) = \frac{\Gamma_{j_a}(n,v)}{\Gamma(n,v)} \tag{2.3}$$

$$P_{j_b}(n,v) = \frac{\Gamma_{j_b}(n,v)}{\Gamma(n,v)} \tag{2.4}$$

$$P_{j_a j_b}(n,v) = \frac{\Gamma_{j_a j_b}(n,v)}{\Gamma(n,v)}, \tag{2.5}$$

where:

$$\Gamma_{j_a}(n,v) = \sum_{j_b} \Gamma_{j_a j_b}(n,v) \tag{2.6}$$

$$\Gamma_{j_b}(n,v) = \sum_{j_a} \Gamma_{j_a j_b}(n,v). \tag{2.7}$$

$$\tag{2.8}$$

The total branching ratios can then be calculated by combining the results of the linewidth and the branching ratios per dissociating state. We treat the photo dissociation process as non-coherent, so we can use the weighted avarage.

$$P_{j_a}^{tot}(v) = \frac{\sum_n P_{j_a}(n,v)\Gamma(n,v)}{\sum_{n j_a} P_{j_a}(n,v)\Gamma(n,v)} \tag{2.9}$$

$$P_{j_b}^{tot}(v) = \frac{\sum_n P_{j_b}(n,v)\Gamma(n,v)}{\sum_{n j_b} P_{j_b}(n,v)\Gamma(n,v)} \tag{2.10}$$

$$P_{j_a j_b}^{tot}(v) = \frac{\sum_n P_{j_a j_b}(n,v)\Gamma(n,v)}{\sum_{n j_a j_b} P_{j_a j_b}(n,v)\Gamma(n,v)}. \tag{2.11}$$

2.2 Potentials

The potentials that were used are taken from Toniolo *et al.* [3]. They used a multireference perturbation CI method, CIPSI (Configuration Interaction by Perburbation with multiconfigurational zeroth-order wave

functions Selected by the Iterative process), for which they used the MO basis produced by closed shell SCF calculations with fluctuating accupation numbers. They used the Dunning's cc-pVTZ basis set, supplemented with diffuse s and p functions on the oxygen atom. The potentials were corrected to make sure they reproduce the experimental values for the interatomic distance of the minimum R_e, the dissociation energy D_e and the energy between the minimum of the $X^2\Pi$ state and the minimum of the $A^2\Pi$ state, T_e. The corrections for respectively the $X^2\Pi$, the $A^2\Pi$ and the other potentials are

$$\begin{aligned} V' &= -1.27e^{-1.6R} + V \\ V' &= -0.001514 - 0.925e^{-1.7R} + V \\ V' &= -0.925e^{-1.7R} + V, \end{aligned}$$

where V are the uncorrected potentials, V' the corrected potentials and R is the interatomic distance. In these equations the energies are in hartree and the distance in bohr. These potentials are plotted in figure 1.1.

For the $A^2\Pi$ state also a Rydberg-Klein-Rees (RKR) potential is available from Howie *et al.* [2]. The vibrational and rotational parameters they derived from fits to the experimental data are shown in table 2.1. These are Dunham parameters, which define the polynomial function from which the shape of the potential

Vibrational parameters		Rotational parameters	
Y_{10}	520.9876	Y_{01}	0.446211
Y_{20}	-8.39095	Y_{11}	-0.009078
Y_{30}	0.16603	Y_{21}	$6.454 \cdot 10^{-4}$
Y_{40}	-0.02484566	Y_{31}	$-7.7825 \cdot 10^{-5}$
Y_{50}	$9.4597 \cdot 10^{-4}$	Y_{41}	$5.23556 \cdot 10^{-6}$
Y_{60}	$-3.11094 \cdot 10^{-5}$	Y_{51}	$-2.2416 \cdot 10^{-8}$
Y_{70}	$1.19938 \cdot 10^{-6}$		
Y_{80}	$-1.86571 \cdot 10^{-8}$		

Table 2.1: The vibrational and rotational parameters for the $A^2\Pi$ state.

can be derived with the RKR procedure [10]. The potential was shifted so that the minimum of the potential lies 31 224.74 cm^{-1} above the $v'' = 0$ of the $X^2\Pi_{3/2}$ state and at $R_e = 1.855$Å. The RKR potential can be reproduced using equation [2.2]:

$$E_{v,J} = \sum_{l,m} Y_{lm} \left(v + \frac{1}{2}\right)^l \Big(J(J+1)\Big)^m. \tag{2.12}$$

In spectroscopy the vibrational parameters Y_{10}, Y_{20}, Y_{30}, and Y_{40} are usually written as ω_e, $-\omega_e x_e$, $\omega_e y_e$ and $-\omega_e z_e$ respectively and the rotational parameters Y_{01}, Y_{11}, and Y_{21} as B_e, $-\alpha_e$ and γ_e respectively. In figure 2.1 it can be seen that there are some differences between the *ab initio* and RKR potentials of $A^2\Pi$.

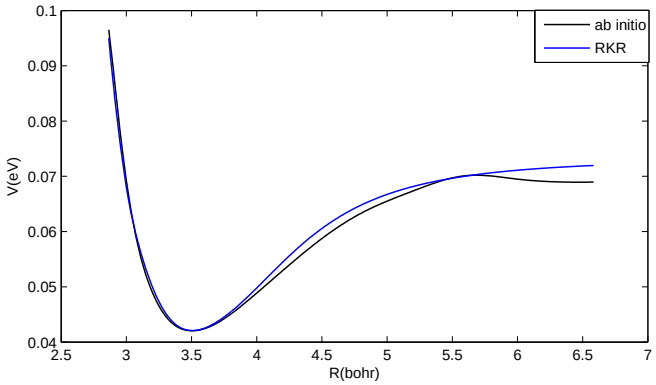

Figure 2.1: The *ab initio* and RKR $A^2\Pi$ potentials.

The *ab initio* potentials still have to be adjusted for the spin-orbit interaction. The spin-orbit splittings A for the $X^2\Pi$ and $A^2\Pi$ states are respectively 320 and 518 cm^{-1} [5]. For $\Omega = 3/2$ both potentials have to be lowered by $0.5A$ and for $\Omega = 1/2$ the potential has to be raised by the same amount. The RKR $A^2\Pi$ potential is determined for the $\Omega = 3/2$ case, so the $\Omega = 1/2$ potential can be approximated by adding 518 cm^{-1}.

2.3 Bases

The coupled channels equations were setup in the molecular basis. To obtain the partial cross sections the S-matrix was transformed to the atomic basis.

Two different bases were used to describe the atoms. The molecular basis, which uses the LS-coupling, also called Russell-Saunders coupling, and the atomic basis. [11]. The calculations were done in the molecular basis, but the results are in the atomic basis, so a transformation matrix was needed.

2.3.1 Molecular Basis

In the molecular basis the individual orbital angular momenta of the electrons l are combined to give the total orbital angular momentum L. In the same way the individual electron spin angular momenta s are combined and give the total spin S. Then L and S can be coupled to make the total angular momentum J. The values of J are between $|L-S|$ and $L+S$. In the same way the projections on the interatomic axis of L and S, Λ and Σ respectively, can be coupled to produce the projection of J, which is called Ω. The value of Ω is given by $\Lambda+\Sigma$.

The O atom has two unpaired p-electrons and therefore $l_a = 1$ and $s_a = 1$. The Cl atom has one unpaired electron, therefore $l_b = 1$ and $s_b = \frac{1}{2}$. This results in $L = 0, 1, 2$ and $S = \frac{1}{2}, \frac{3}{2}$ and they couple together to $J = \frac{1}{2}, \frac{3}{2}, \frac{5}{2}, \frac{7}{2}$. The projections become $\Lambda = 0, \pm1, \pm2$, $\Sigma = \pm\frac{1}{2}, \pm\frac{3}{2}$ and $\Omega = \pm\frac{1}{2}, \pm\frac{3}{2}, \pm\frac{5}{2}, \pm\frac{7}{2}$. The dimension of the molecular basis of ClO is 54. The notation of this basis in the angular momentum theory is:

$$|(l_a l_b)L\Lambda(s_a s_b)S\Sigma\rangle. \tag{2.13}$$

2.3.2 Atomic Basis

In the atomic basis l and s are first combined to become the angular momentum j and after that the individual j's are coupled to give J. Also the projections λ and σ are combined to ω and then the ω's are coupled to Ω.

For O $j_a = 0, 1, 2$ and for Cl $j_b = \frac{1}{2}, \frac{3}{2}$, which results in $J = \frac{1}{2}, \frac{3}{2}, \frac{5}{2}, \frac{7}{2}$. The projections become $\omega_a = 0, \pm1, \pm2$, $\omega_b = \pm\frac{1}{2}, \pm\frac{3}{2}$ and $\Omega = \pm\frac{1}{2}, \pm\frac{3}{2}, \pm\frac{5}{2}, \pm\frac{7}{2}$. The dimension of the atomic basis of ClO is also 54. The notation of this basis in the angular momentum theory is:

$$|(l_a s_a)j_a\omega_a(l_b s_b)j_b\omega_b\rangle. \tag{2.14}$$

2.3.3 Transformation Matrix

The transformation matrix is used to transform the atomic basis to the molecular basis. We write this matrix as $\langle j_a\omega_a j_b\omega_b|L\Lambda S\Sigma\rangle$. Using the following equations we can write this in terms of l_a, l_b, s_a and s_b:

$$\begin{aligned}
|L\Lambda\rangle &= \sum_{\lambda_a\lambda_b} |l_a\lambda_a\rangle|l_b\lambda_b\rangle\langle l_a\lambda_a l_b\lambda_b|L\Lambda\rangle \\
|S\Sigma\rangle &= \sum_{\sigma_a\sigma_b} |s_a\sigma_a\rangle|s_b\sigma_b\rangle\langle s_a\sigma_a s_b\sigma_b|S\Sigma\rangle \\
|j_a\omega_a\rangle &= \sum_{\lambda_a\sigma_a} |l_a\lambda_a\rangle|s_a\sigma_a\rangle\langle l_a\lambda_a s_a\sigma_a|j_a\omega_a\rangle \\
|j_b\omega_b\rangle &= \sum_{\lambda_b\sigma_b} |l_b\lambda_b\rangle|s_b\sigma_b\rangle\langle l_b\lambda_b s_b\sigma_b|j_b\omega_b\rangle.
\end{aligned}$$

Here $\langle a\alpha b\beta|c\gamma\rangle$ is a Clebsch-Gordan coefficient [12]. This results in:

$$\begin{aligned}
\langle(l_a s_a)j_a\omega_a(l_b s_b)j_b\omega_b|(l_a l_b)L\Lambda(s_a s_b)S\Sigma\rangle = \sum_{\lambda_a\lambda_b\sigma_a\sigma_b} \quad & \langle l_a\lambda_a|\langle s_a\sigma_a|\langle l_b\lambda_b|\langle s_b\sigma_b|\langle j_a\omega_a|l_a\lambda_a s_a\sigma_a\rangle\langle j_b\omega_b|l_b\lambda_b s_b\sigma_b\rangle \\
& |l_a\lambda_a\rangle|l_b\lambda_b\rangle|s_a\sigma_a\rangle|s_b\sigma_b\rangle\langle l_a\lambda_a l_b\lambda_b|L\Lambda\rangle\langle s_a\sigma_a s_b\sigma_b|S\Sigma\rangle.
\end{aligned}$$

With $\sum_{\lambda_a}\langle l_a\lambda_a|l_a\lambda_a\rangle = 1$ this leads to:

$$\begin{aligned}
\langle(l_a s_a)j_a\omega_a(l_b s_b)j_b\omega_b|(l_a l_b)L\Lambda(s_a s_b)S\Sigma\rangle = \sum_{\lambda_a\lambda_b\sigma_a\sigma_b} \quad & \langle j_a\omega_a|l_a\lambda_a s_a\sigma_a\rangle\langle j_b\omega_b|l_b\lambda_b s_b\sigma_b\rangle \\
& \langle l_a\lambda_a l_b\lambda_b|L\Lambda\rangle\langle s_a\sigma_a s_b\sigma_b|S\Sigma\rangle.
\end{aligned} \tag{2.15}$$

The summations over $\lambda_a, \lambda_b, \sigma_a$ and σ_b can be done using some angular momentum algebra [12]. The result is

$$\langle j_a \omega_a j_b \omega_b | L\Lambda S\Sigma\rangle = \sum_J \sqrt{(2j_a+1)(2j_b+1)(2L+1)(2S+1)} \langle j_a \omega_a j_b \omega_b | J\Omega\rangle \langle J\Omega | L\Lambda S\Sigma\rangle \begin{Bmatrix} l_a & s_a & j_a \\ l_b & s_b & j_b \\ L & S & J \end{Bmatrix}, \tag{2.16}$$

where the last factor is a $9j$-symbol.

2.4 Quadrupole-Quadrupole Interaction

For the molecular basis we need to assign a total orbital angular momentum L to the potentials asymptotically. For a configuration of atomic orbitals with orbital quantum numbers l_i, coupled to a total angular momentum L, we have

$$\hat{\sigma}_v(xz)|L\Lambda\rangle = (-1)^{L+\Lambda+\sum_i l_i}|L,\Lambda\rangle. \tag{2.17}$$

Taking into account the $(3p)^5$ configuration of Cl and the $(2p)^4$ configuration of O, we find that the $|L=1,\Lambda=0\rangle$ state is a Σ^+ state, while the two Σ^- states correlating with the Cl(^{2}P) and O(^{3}P) limit correspond to $L=0$ and $L=2$. The quadrupole-quadrupole interaction determines the energy ordering of these states. As described in [6] the matrix elements of the quadrupole-quadrupole interaction term $\hat{V}_5$ are

$$\langle L\Lambda|\hat{V}_5|L\Lambda\rangle = R^{-5}\frac{3}{2}\sqrt{70}Q_{zz}^{(O)}Q_{zz}^{(Cl)}(-1)^{L-\Lambda}\langle L,\Lambda,L,-\Lambda|4,0\rangle, \tag{2.18}$$

where R is the interatomic distance and $Q_{zz}^{(i)}$, $i=$ Cl, O are the quadrupole moments of the $\Lambda_i=0$ components of the atoms. This equation shows that the relative signs of the quadupole moments of Cl and O are required to determine the energy ordering. From the electronic configurations of Cl and O atoms, we observe that the quadrupole moments must have opposite signs: three electrons in different 2p orbitals give a spherical contribution to the charge distribution. Therefore, for the O atom the quadrupole moment is determined by the fourth 2p electron, while in Cl the quadrupole moment arises from a hole in the 3p shell. The Clebsch-Gordan coefficient in the equation is non-zero only for $L=2$ and is positive for each value of Λ. Hence, we arrive at the assignments for the molecular states shown in table 2.2.

$L\Lambda$	0	1	2
0	$2^{2,4}\Sigma^-$		
1	$1^{2,4}\Sigma^+$	X$^2\Pi$, $1^4\Pi$	
2	$1^{2,4}\Sigma^-$	$3^2\Pi$, $2^4\Pi$	$1^{2,4}\Delta$

Table 2.2: All molecular states arising from the Cl(^{2}P) + O(^{3}P) atomic limit.

2.5 Atomic Spin-Orbit Coupling

The atomic spin-orbit coupling is expressed by:

$$\hat{H}_{so} = \zeta \hat{L}\cdot\hat{S}, \tag{2.19}$$

where ζ is the spin-orbit parameter. And since

$$\hat{J}^2 = \left(\hat{L}+\hat{S}\right)^2 = \hat{L}^2 + 2\hat{L}\cdot\hat{S} + \hat{S}^2, \tag{2.20}$$

this results in:

$$\hat{H}_{so} = \frac{\zeta}{2}\left(\hat{J}^2 - \hat{L}^2 - \hat{S}^2\right) = \frac{1}{2}\left(J(J+1) - L(L+1) - S(S+1)\right). \tag{2.21}$$

If we assume the spin-orbit interaction of the molecules is the combination of the spin-orbit interaction of the atoms, we get the following expressing for diatoms:

$$\hat{H}_{so} = \frac{A}{2}(j_a(j_a+1) - l_a(l_a+1) - s_a(s_a+1)) + \frac{B}{2}(j_b(j_b+1) - l_b(l_b+1) - s_b(s_b+1)). \tag{2.22}$$

Here A is the spin-orbit coupling of O and B of Cl, which are -76 and -588 cm^{-1} respectively.

Coupling matrix element	Ratio of magnitudes of $\Omega = 3/2$ coupling to $\Omega = 1/2$ coupling
$\langle {}^4\Sigma^-\|H_{so}\|{}^2\Pi\rangle$	$\frac{1}{\sqrt{3}}$
$\langle {}^4\Sigma^+\|H_{so}\|{}^2\Pi\rangle$	$\frac{1}{\sqrt{3}}$
$\langle {}^2\Pi\|H_{so}\|{}^2\Pi\rangle$	1
$\langle {}^4\Pi\|H_{so}\|{}^2\Pi\rangle$	1
$\langle {}^4\Delta\|H_{so}\|{}^2\Pi\rangle$	$\sqrt{3}$

Table 2.3: The ratios of the coupling constants between the $A^2\Pi$ state and the repulsive states.

The H_{so}-matrix elements become:

$$\langle\psi(i)|\hat{H}_{so}|\psi(j)\rangle = \left(\frac{A}{2}(j_a(i)(j_a(i)+1) - l_a(l_a+1) - s_a(s_a+1)) + \frac{B}{2}(j_b(j)(j_b(j)+1) - l_b(l_b+1) - s_b(s_b+1))\right)\delta_{i,j}, \tag{2.23}$$

where $\psi(i)$ and $\psi(j)$ are the basisvectors of the atomic basis and $j_a(i)$ and $j_b(i)$ are the values of j_a and j_b respectively of the basisvector $\psi(i)$. The calculations are done in the molecular basis, which means the H_{so}-matrix has to be transformed using the transformation matrix described in equation (2.16)

$$H'_{so} = \langle L\Lambda S\Sigma|j_a\omega_a j_b\omega_b\rangle\langle j_a\omega_a j_b\omega_b|\hat{H}_{so}|j_a\omega_a j_b\omega_b\rangle\langle j_a\omega_a j_b\omega_b|L\Lambda S\Sigma\rangle = U^\dagger H_{so} U. \tag{2.24}$$

2.6 Spin orbit coupling

The coupling between the states, $\hat{V}_{10}$ in equation (2.1) can be spin orbit coupling or an avoided crossing. If there is spin orbit coupling between the $A^2\Pi$ state and the dissociative state, the Wigner-Eckart theorem will give the following relation between the different Ω components for Hund's case A diatomic molecules [5]:

$$\langle nS\Lambda\Sigma|H_{SO}(R)|n'S'\Lambda'\Sigma'\rangle = (-1)^{S-\Sigma}\begin{pmatrix} S & 1 & S' \\ -\Sigma & \Delta\Sigma & \Sigma' \end{pmatrix} \times C_1\langle nS\Lambda\|H_{SO}(R)\|n'S'\Lambda'\rangle. \tag{2.25}$$

The ratios of the magnitudes of $\Omega = 3/2$ coupling and $\Omega = 1/2$ coupling are in table 2.3. There can be no coupling between the $A^2\Pi$ state and the $^2\Sigma$ states for $\Omega = 3/2$ and the $A^2\Pi$ state and the $^2\Delta$ states for $\Omega = 1/2$. Between the $A^2\Pi$ state $3^2\Pi$ states there is an avoided crossing.

2.7 Sinc-DVR

The sinc-DVR [13], sinc discrete variable representation, is used to calculate the vibrational wave functions ψ_i, which can be used to calculate the linewidth by using equation [2.1]. To use this representation the grid points have to be equally spaced.

2.8 Numerov Algorithm

The numerov algorithm is used to solve the coupled channel equation. The wavefunction Ψ_i, at gridpoint i, can also be expressed in terms of Ψ_{i+1}:

$$\Psi_i = Q_{i+1}\Psi_{i+1}. \tag{2.26}$$

This leads to the recursion relation for the coefficients Q_i:

$$Q_{i+1} = \frac{C_{i+1}}{12 - 10C_i - C_{i-1}Q_i}, \tag{2.27}$$

with:

$$C_i = 1 - \frac{\Delta^2}{12}\left(-\frac{2\mu}{\hbar^2}(E - V_i)\right), \tag{2.28}$$

where Δ is the grid spacing. If we assume that $\Psi_0 = 0$, all the values of Ψ and Q_i can be computed.

Chapter 3

Results

3.1 Vibrational Levels

The vibrational levels of the $A^2\Pi$ state are given in table 3.1. The first column are the vibrational levels we have calculated using the *ab initio* potential from Toniolo *et al.* [3]. The second column are the levels we calculated using the RKR potential from Howie *et al.* [2] and the third are the results from their experiments, which they used to make their potential. As expected the differences between the levels of the RKR and the experimental results are very small. The differences between the *ab initio* and experiment are bigger, but not bigger than expected. The difference is 6.9% at $v' = 1$, becomes smaller with each vibrational levels until it is 2.5% at $v' = 16$. For vibrational levels $v' = 17$ and $v' = 18$ the differences are respectively 3.9% and 5.2%.

v'	*ab initio*	RKR	experiment [2]
0	0.00	0.00	0.00
1	470.01	504.04	504.63
2	929.54	992.43	993.32
3	1372.78	1465.12	1466.09
4	1799.90	1921.69	1923.58
5	2210.90	2361.43	2362.15
6	2607.25	2783.42	2783.89
7	2989.06	3186.58	3186.76
8	3355.96	3569.70	3569.58
9	3706.96	3931.54	3931.13
10	4040.69	4270.85	4270.22
11	4355.63	4586.47	4585.71
12	4650.17	4877.41	4876.63
13	4923.17	5142.90	5142.20
14	5176.36	5382.48	5381.95
15	5414.05	5596.04	5595.71
16	5638.97	5783.83	5783.70
17	5713.01	5946.52	5946.54
18	5769.57	6085.19	6085.30

Table 3.1: The energy difference of the vibrational levels with the $v = 0$ level of the $A^2\Pi$ state in cm^{-1}.

3.2 Spin-Orbit Coupling

The spin-orbit couplings between the dissociating states and the $A^2\Pi$ state were calculated using MOLPRO [14]. This program uses the state-interacting method with the Breit-Pauli operator. In this method the spin-orbit eigenstates are obtained by diagonalising $\hat{H}_{el} + \hat{H}_{so}$ in a basis of eigenfunctions of $\hat{H}_{el}$. Since $\Delta\Omega = 0$ and $\Omega = \Sigma + \Lambda$, the selection rule for the spin-orbit coupling for the z-axis (interatomic axis) is:

$$\Delta\Sigma = 0 \tag{3.1}$$

and for the x and y-axis is:

$$\Delta\Sigma = \pm 1. \tag{3.2}$$

We have used group theory to determine the selection rules of the spin-orbit coupling. All diatoms have $C_{\infty v}$ symmetry, but MOLPRO uses the abelian subgroup C_{2v}, of which the character table is shown in table 3.2. This means that the Π-states have symmetry label B_1 or B_2, the Δ-states A_1 or A_2, the Σ^+-states have

	E	C_2	σ_v	σ'_v	linear, rotations	quadratic
A_1	1	1	1	1	z	x^2, y^2, z^2
A_2	1	1	−1	−1	R_z	xy
B_1	1	−1	1	−1	x, R_y	xz
B_2	1	−1	−1	1	y, R_x	yz

Table 3.2: The character table of the C_{2v} group.

symmetry label A_1 and the Σ^--states A_2. This results in the symmetries and selection rules as shown in table 3.3.

$^2\Pi$ couples with	symmetry product	axis	selection rule
Π	A_1 or A_2	z	$\Delta\Omega = 0$
Δ	B_1 or B_2	x or y	$\Delta\Sigma = \pm 1$
Σ^+	B_1 or B_2	x or y	$\Delta\Sigma = \pm 1$
Σ^-	B_1 or B_2	x or y	$\Delta\Sigma = \pm 1$

Table 3.3: The selection rules for the couplings with the $A^2\Pi$ state.

The spin-orbit couplings have been computed using MCSCF followed by CI with single/double excitations. This has been done for several interatomic distances between 3.2 and 4.2 bohr, using a contracted aug-pVTZ basis as can be seen in figure 3.1.

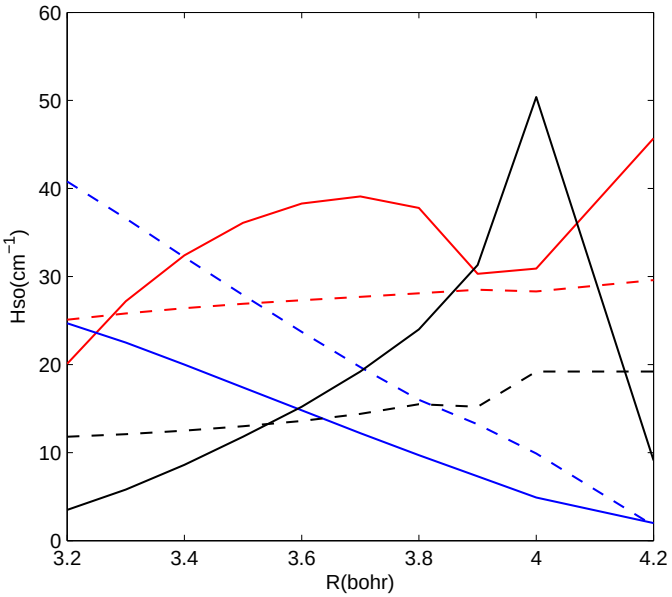

Figure 3.1: The spin-orbit coupling constants between the $A^2\Pi$ state and the dissociative electronic states depending on the interatomic distance for $\Omega = 3/2$. The blue line is $1^4\Delta$, the blue dashed line $1^4\Sigma^+$, the black line $3^2\Pi$, the black dashed line $1^4\Pi$, the red line $2^4\Sigma^-$ and the red dashed line $1^2\Delta$.

The computed spin-orbit couplings at a given R have the $\Omega = \frac{3}{2}/\Omega = \frac{1}{2}$ ratio predicted by use of the Wigner-Eckart theorem[Eq.(2.25)]. The values that have been calculated at the crossing distance are given in table 3.4. There also the couplings that were used by Toniolo *et al.* [3] and Lane *et al.* [5] have been given. All values in the table are in cm^{-1}.

The couplings by Lane *et al.* were derived by fitting the results to the experimental results for $\Omega = 3/2$ after which they have used the Wigner-Eckart theorem to get the results for $\Omega = 1/2$. The results of Toniolo *et al.*

	$\Omega = 3/2$			$\Omega = 1/2$		
	this work	Toniolo *et al.* [3]	Lane *et al.* [5]	this work	Toniolo *et al.*	Lane *et al.*
$\langle 3^2\Pi \vert H_{so} \vert ^2\Pi\rangle$	8	12	125	8	128	125
$\langle 1^4\Pi \vert H_{so} \vert ^2\Pi\rangle$	15	23		15	19	
$\langle 2^4\Pi \vert H_{so} \vert ^2\Pi\rangle$	51	1		51	10	
$\langle 1^4\Delta \vert H_{so} \vert ^2\Pi\rangle$	13	28		22	46	
$\langle 1^4\Sigma^+ \vert H_{so} \vert ^2\Pi\rangle$	20	13	50	11	38	29
$\langle 2^4\Sigma^- \vert H_{so} \vert ^2\Pi\rangle$	25	69	82	15	27	47
$\langle 1^2\Delta \vert H_{so} \vert ^2\Pi\rangle$	26	57				
$\langle 1^2\Sigma^+ \vert H_{so} \vert ^2\Pi\rangle$				17	33	
$\langle 1^2\Sigma^- \vert H_{so} \vert ^2\Pi\rangle$				4	6	
$\langle 2^2\Sigma^- \vert H_{so} \vert ^2\Pi\rangle$				1	4	

Table 3.4: The spin-orbit coupling constants between the $A^2\Pi$ state and the dissociative electronic states.

have been computed, but they do not have the predicted Ω-ratio. This can be the result of the dependence of the spin-orbit couplings on the interatomic distance. The crossing of the $A^2\Pi$ state with the dissociative states occur at a different interatomic distance for $\Omega = 1/2$ than for $\Omega = 3/2$. Figure 3.1 shows the dependence for all the states with $\Omega = 3/2$ (except $2^4\Pi$ to avoid scaling). The difference in interatomic distance can therefore change the spin-orbit coupling constant. For the $1^4\Delta$, $2^4\Sigma^-$ and $1^2\Delta$ states this dependence alone does not explain the deviations from the Wigner-Eckart theorem. Since no details were given on method they have used to compute these couplings, we do not know why there is a difference. The crossing of the $3^2\Pi$ state and the $A^2\Pi$ state is an avoided crossing, which Toniolo *et al.* calculated to be 112 cm^{-1}.

3.3 Linewidth

There have been several experimental studies of the linewidth for different vibrations of the $A^2\Pi$ state. Most studies focussed on $\Omega = 3/2$, but Howie *et al.* [2] also have some results for $\Omega = 1/2$. The experimental results are shown in table 3.5 with all values in cm^{-1}.

Lane *et al.* [5] have used their potentials, including the RKR-potential we have used, to calculate the predissociation rates of the $A^2\Pi$ via several repulsive states. They have fitted these rates to the total experimental results for $v = 0-6$, to obtain the couplings. The rates they found agree well with the present results, although our rates for the $1^4\Sigma^+$ state agree better with their $1^4\Delta$ and vice versa. The reason for this is that the potentials of these repulsive states are very much alike, which results in rates that are much alike too. They also have the same symmetry in C_2v and it is therefore difficult to keep them apart. The potentials of the $2^4\Sigma^-$ and $1^4\Pi$ states are also very similar, which was the reason for Lane to leave the 1 $^4\Pi$ potential out of their simulation. Our rates for these states are also very similar, but because we computed the couplings we were still able to use both rates. Our rates that were obtained using the RKR potential agree better with their results.

Toniolo *et al.* have used their *ab initio* potentials to compute the theoretical linewidth for several rovibrational levels of the $A^2\Pi$ state [3]. We have computed the linewidth by using their potentials and couplings. Most of our results are in reasonable agreement with theirs, except those of the dissociating states $2^4\Pi$ and $2^4\Sigma^-$. When a coupling of 20 cm^{-1} is used instead of 1 cm^{-1} for the coupling between $A^2\Pi$ and $2^4\Pi$, the computed linewidths are of the same order as Toniolo's, but shifted by 3 vibrational quanta. The computed results of $2^4\Sigma^-$ has the different vibrational dependence as Toniolo's, see figure 3.2. The total linewidth results computed either by Toniolo or ourselves using these potentials and couplings do not fit the experimental results very well, as can be seen in figure 3.3. Their results are similar to ours for $1^4\Sigma^+$ and $1^4\Delta$ states, but not for the $2^4\Sigma^-$ and $1^4\Pi$ states, which suggests that there may also be some other difference between our calculation and theirs for the $2^4\Sigma^-$ state. Our rates that were obtained using only the *ab initio* potentials are in better agreement with their results.

The predissociation rates of the $A^2\Pi$ have also been computed the same way for $\Omega = \frac{1}{2}$, but it is harder to draw conclusions for there are very few experimental results. The differences between our and Toniolo's results which we have described above for $\Omega = \frac{3}{2}$, we have also seen for $\Omega = \frac{1}{2}$. Only the coupling for $2^4\Pi$ gives results of the same order as theirs. When comparing the results with Lane's, we draw the same conclusions for $\Omega = \frac{1}{2}$ as for $\Omega = \frac{3}{2}$.

For all the calculations of the predissociation rates we find that there is little difference between the results for the Hund's case (a) and (c) calculations. From the differences between the results using the RKR versus the *ab initio* $A^2\Pi$ potential we come to the same conclusion as Lane *et al.* that shifting or slightly changing the shape of a potential has a big influence on the predissociation rates. Using the RKR potential gives the best

	$\Omega = 3/2$			$\Omega = 1/2$
v	McLoughlin [7]	Howie [2]	Barton [8]	Howie
0		1.2(4)		
1		2.65(35)		
2		2.7(2)		$0.85^{(+35)}_{(-25)}$
3		5.45(35)	5.66	2.65(35)
4		4.15(25)	4.09(5)	3.05(15)
5		6.35(35)	6.00(10)	8(1)
6		10(1)	10.00	$10^{(+4)}_{(-3)}$
7	5.00(100)	5.0(2)	5.21(17)	
8	4.62(92)		4.76(8)	
9	4.92(98)		5.15(8)	
10	5.79(116)		5.63	
11	2.35(47)		3.58	
12	3.68(74)		3.75	
13	5.43(109)			
14	2.77(55)			
15	2.08(42)			
16	1.82(36)			
17	1.05(21)			
18	1.75(35)			
19	0.40(8)			
20	0.52(10)			
21	0.52(10)			
22	0.76(15)			
23	0.53(11)			

Table 3.5: The experimental linewidth results.

total results, but it is possible that even better results can be obtained by shifting the dissociating potentials. The couplings obtained by Lane give the best results for low vibrations. They fitted the couplings to fit the results for low vibrations, so this was expected. Our results, which can be seen in figure 3.3, have correctly predicted the main peak of the linewidth at $v' = 6$. Only at $v' = 5$ we have overestimated the linewidth. At $v' = 1, 2, 3, 7, 9, 12$ and 13 we have largely underestimated the linewidth. Changing the couplings will also change the linewidth and the location of the peak.

3.4 Fine Structure Branching Ratios

In table 3.6 are described our best results and the experimental results. The fine structure branching ratios for the individual dissociating states differ only slightly between the case (a) and (c) calculations. When using the case (c) the effects of changing the vibrational quantum number are smoother. The difference between the RKR and *ab initio* potentials is the vibrational number at which the branching ratios are at their maximum or minimum. When calculating the total branching ratios [Eq.(2.9-2.11)] for all the states the differences between using the RKR and *ab initio* is even smaller. The differences between the case (a) and (c) are more obvious. The largest influence on the branching ratios are the coupling constants.

The fine structure branching ratios have been obtained experimentally in 2006 by Kim *et al.* for $v = 6-11$ [6]. For $v = 0 - 5$ we have used the results by Dooley *et al.* [1]. We have compared the results of the calculations with the experimental results for $v' = 0 - 11$ using the root mean square error.

The results of the case (c) calculation using our coupling constants as in table 3.4 and the RKR potential have a root mean square (rms) error of 1.23. When we also use the avoided crossing coupling between the $A^2\Pi$ and $3^2\Pi$ states, the rms error drops to 1.09, which results are described in table 3.6 and figures figure 3.4 and 3.5. This is slightly better than the case (a) calculations, where we get a rms error of 1.11 when we use the same coupling constants and potential. The case (c) calculation with these constants and the *ab initio* potential gives an rms error of 1.12. The differences between the results become greater when we use a different set of coupling constants. When using Toniolo's or Lane's constants the rms error goes from 1.09 to respectively 1.23 and 1.48. The results of a diabatic calculation by Kim *et al.* [6] are only for $v' = 6 - 11$ and do not have such a good agreement with the experiment as our results and are included in figures 3.4 and 3.5.

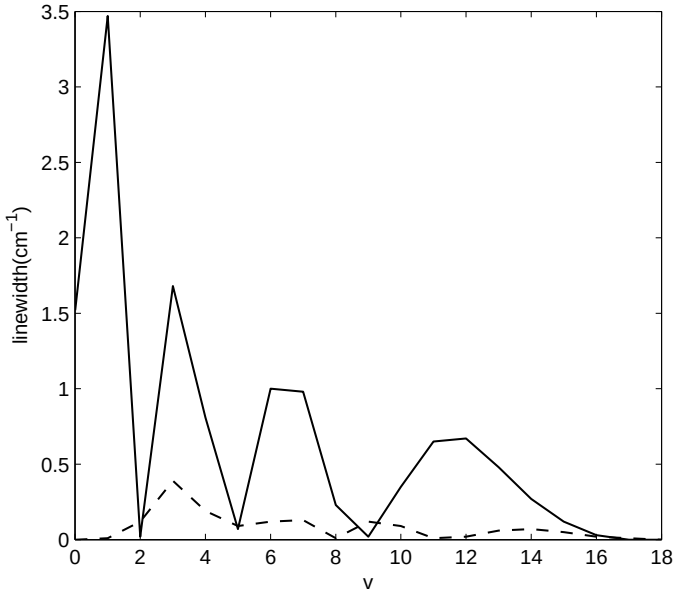

Figure 3.2: The linewidth through the $2^4\Sigma^-$ channel. The black line are the results of the calculations of Toniolo [3] and the dashed line are our results.

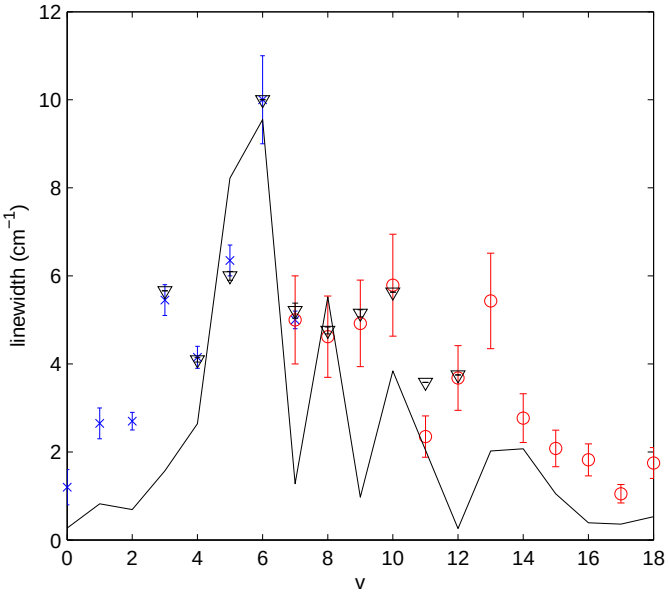

Figure 3.3: The total linewidth results of our calculations using the RKR potential. The black line are the results of the calculations. The blue crosses are the experimental results by Howie the red circles are the experimental results by McLoughlin and the black triangles are the experimental results by Barton.

v'	O($^3P_0$) Cl($^2P_{1/2}$)	O($^3P_1$) Cl($^2P_{1/2}$)	O($^3P_2$) Cl($^2P_{1/2}$)	O($^3P_0$) Cl($^2P_{3/2}$)	O($^3P_1$) Cl($^2P_{3/2}$)	O($^3P_2$) Cl($^2P_{3/2}$)
0	0.00 (0.00)	0.02 (0.10)	0.15 (0.37)	0.04 (0.06)	0.36 (0.37)	0.43 (0.10)
1	0.00 (0.00)	0.02 (0.00)	0.15 (0.31)	0.04 (0.06)	0.34 (0.56)	0.44 (0.07)
2	0.00 (0.00)	0.03 (0.07)	0.26 (0.37)	0.09 (0.04)	0.28 (0.29)	0.34 (0.24)
3	0.00 (0.00)	0.04 (0.00)	0.25 (0.09)	0.12 (0.24)	0.28 (0.41)	0.32 (0.26)
4	0.00 (0.00)	0.13 (0.00)	0.15 (0.12)	0.24 (0.33)	0.27 (0.35)	0.21 (0.21)
5	0.00 (0.00)	0.18 (0.16)	0.10 (0.08)	0.28 (0.26)	0.26 (0.22)	0.18 (0.28)
6	0.00 (0.00)	0.21 (0.22)	0.10 (0.18)	0.26 (0.26)	0.25 (0.15)	0.18 (0.19)
7	0.00 (0.02)	0.26 (0.34)	0.24 (0.02)	0.07 (0.22)	0.19 (0.19)	0.24 (0.22)
8	0.00 (0.03)	0.16 (0.21)	0.07 (0.10)	0.29 (0.32)	0.27 (0.24)	0.21 (0.09)
9	0.00 (0.00)	0.29 (0.30)	0.22 (0.18)	0.07 (0.06)	0.18 (0.17)	0.24 (0.29)
10	0.00 (0.00)	0.17 (0.16)	0.08 (0.26)	0.26 (0.13)	0.26 (0.21)	0.23 (0.24)
11	0.00 (0.00)	0.12 (0.00)	0.07 (0.31)	0.28 (0.13)	0.28 (0.37)	0.25 (0.19)
12	0.00	0.38	0.19	0.06	0.15	0.22
13	0.00	0.17	0.07	0.26	0.26	0.24
14	0.00	0.11	0.06	0.29	0.28	0.26
15	0.00	0.14	0.08	0.26	0.26	0.26
16	0.00	0.36	0.18	0.09	0.15	0.21
17	0.00	0.38	0.17	0.09	0.14	0.21
18	0.00	0.23	0.09	0.20	0.22	0.25

Table 3.6: The fine branching ratio of the case (c) calculations using the RKR potential. Between the parentheses are the results of the experiments.

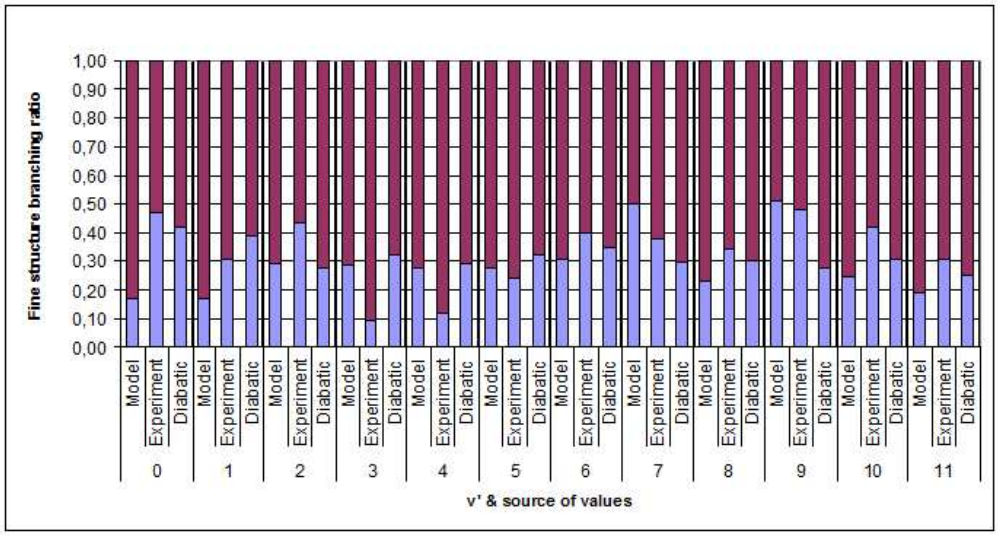

Figure 3.4: The fine branching ratios of this work, the experiment [1] and the diabatic calculation [6]. In this figure blue represents $Cl^2P_{1/2}$ and purple $Cl^2P_{3/2}$.

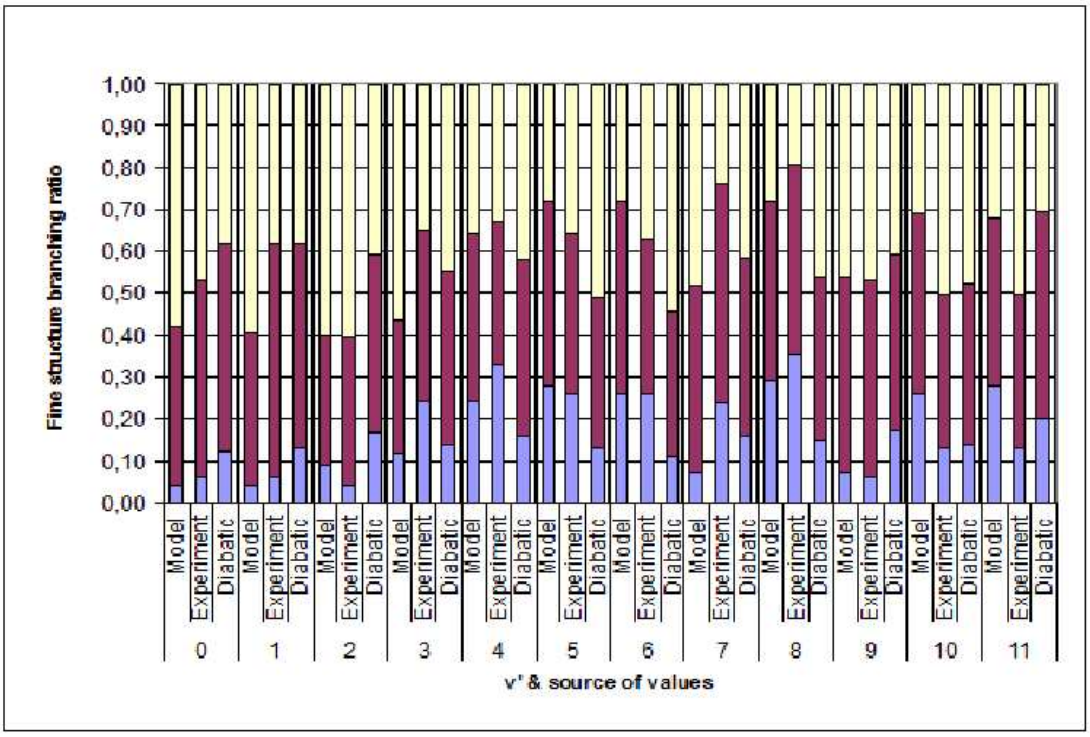

Figure 3.5: The fine branching ratios of this work, the experiment [1] and the diabatic calculation [6]. In this figure blue represents O^3P_0, purple O^3P_1 and yellow O^3P_2.

Chapter 4

Conclusion

The predissociation of ClO in the $A^2\Pi$ state is due to crossings with several repulsive states. The most effective states are the $3^2\Pi$, $2^4\Pi$ and $1^2\Delta$ for $\Omega = 3/2$ and $3^2\Pi$, $2^4\Pi$ and $1^2\Sigma^+$ for $\Omega = 1/2$. The RKR potential produced vibrational levels which are very close to the experimental levels and a lot better than the *ab initio* $A^2\Pi$ potential. The linewidth and fine structure branching ratio results of the RKR potential agree also better with the experimental results than the results of the *ab initio* potential.

The three sets of coupling constants we have looked at during this project are all very different. The couplings used by Lane *et al.* gave the best agreement with experimental linewidth results, while our couplings agreed better with the experimental results of the branching ratios and still reproduced the main peak of the experimental linewidth results. Our results were a bit better than the diabatic results when looking at the branching ratios.

The coupling constants have the largest influence on both the linewidth and branching ratios. Differences in the potentials as shifting or changing the shape of the potential have also a large influence on the linewidth, but only a small influence on the branching ratios. The differences of the linewidth and branching ratios between the Hund's case (a) and (c) calculations are very small.

It is very important to have a good set of potentials to do these calculations, since changing the potentials in any way will make a large difference to the linewidth. Also shifting the potentials can also change the coupling constants, which will change the results of the linewidth and the branching ratio calculations. It could also be useful to take another look at the coupling constants, the three sets now available are all very different. A better understanding of the method Toniolo *et al.* used to produce their set, could help in understanding why their set is much different from ours and might make it possible to improve our set.

Appendix A

Program

A.1 Input

The program was written in SCILAB [15] using routines written by Gerrit Groenenboom. It consists of 10 files with functions and 5 files that run the program. For each calculation a new file is needed that has the input information and specifies what sort of job it is. The input information has to be put in a list which can be given any name, but for this project the name `par` was used. The information that should be included in the list can be seen in table A.1. Also the potentials should be loaded, which can be done by making a function to load them. The list with the input information and the matrix with the potentials can be put into the program. This is done by calling one of the functions `main_photo1, main_photo2, main_photo3` and `main_photo4`, which start the respective calculations of the lifetimes for case (c), the lifetimes for case (a), the branching ratios for case (a), the branching ratios for case (c).

Name	Description
`title`	String that will be put in the output
`outfile`	Name of the file that will hold the values of the parameters and results
`Es`	ψ_E, Vector with the energy grid
`mu`	Reduced mass of the molecule
`dr`	Gridspacing of the distance grid
`grid`	ψ_i, Vector with the distance grid
`R`	Distance which is used for the quadrupole-quadruole interaction
`func`	Vector which controls the spin-orbit coupling per gridpoint
`maxrg`	Maximum distance used for the sinc-dvr calculation
`ngmax`	Maximum vibration quantum number + 1
`A`	Spin-orbit coupling of atom A in E_h
`B`	Spin-orbit coupling of atom B in E_h
`Q1`	Quadrupole moment of atom A
`Q2`	Quadrupole moment of atom B
`la`	l_a, Orbital angular momentum of atom A
`sa`	s_a, Spin angular momentum of atom A
`lb`	l_b, Orbital angular momentum of atom B
`sb`	s_b, Spin angular momentum of atom B
`L1`	L, Total orbital angular momentum of the excited bonding potential
`S1`	S, Total spin angular momentum of the excited bonding potential
`Lambda1`	Λ, Projection of the total orbital angular momentum of the A state
`Omega1`	Ω, Projection of the total angular momentum of the A state
`L2`	L, Total orbital angular momentum of the dissociative state
`S2`	S, Total spin angular momentum of the dissociative state
`Lambda2`	Λ, Projection of the total orbital angular momentum of the dissociative state
`Omega2`	Ω, Projection of the total angular momentum of the dissociative state

Table A.1: The input information needed to do a calculation using the program.

A.2 Output

The results of the program will be put in the outputfile with the name set in the input information. Using SCILAB [15] the information from the outputfile can be retrieved. The results will be in a list, which is given is table A.2. The branching ratios calculations also makes figures where the branching ratios are plotted against the vibration quantum numbers.

Name	Description
`V`	Matrix with the potentials on the grid points
`V2`	Vector with the excited potential on the grid points
`vbas`	List with information on the potentials like L, Λ and S
`vbas2`	Vector with information on the excited potential like L, Λ and S
`nb`	Size of the molecular basis
`ib`	Vector which couples the basisvectors of the molecular basis to its potential
`Ue`	Matrix with the eigenfunctions of the excited state at the vibrational quantum numbers
`Ee`	Vector with the eigenvalues of the excited state at the vibrational quantum numbers
`indv`	Vector that matches the molecular basis vectors to a potential
`mbas`	List with the information of the molecular basis
`abas`	List with the information of the atomic basis
`U`	Transformationmatrix which transforms the atomic basis into the molecular basis
`Hqq`	Matrix with the results of the quadrupole-quadrupole interaction
`Hso`	Matrix with the results of the spin-orbit coupling
`es`	Vector with the energies of the spin-orbit coupling for the atomic basisvectors
`ne`	Amount of gridpoints used for the sinc-dvr calculation
`CS`	List with the cross sections
`indops`	List with open channels
`PVja`	Matrix with the branching ratios of j_a
`PVjb`	Matrix with the branching ratios of j_b
`PVjs`	Matrix with the branching ratios of the j_a and j_b
`mu`	Reduced mass of the molecule

Table A.2: The output information from a calculation done by the program.

Bibliography

[1] Kristin S. Dooley, Michael P. Grubb, Justine Geidosch, Marloes A. van Beek, Gerrit C. Groenenboom, and Simon W. North. Correlated fine structure branching ratios arising from state-selected predissociation of clo ($a^2\pi_{3/2}$). *pccp*, 11:4770–4776, 2009.

[2] Wendy H. Howie, Ian C. Lane, Stuart M. Newman, David A. Johnson, and Andrew J. Orr-Ewing. The uv absorption of clo part 1. *pccp*, 1:3079–3085, 1999.

[3] A. Toniolo, M. Persico, and D. Pitea. An ab initio study of spectroscopy and predissociation of clo. *jcp*, 112(6):2790–2797, 2000.

[4] Hahkjoon Kim, Jiho Park, Tracy C. Niday, and Simon W. North. The uv photodissociation dynamics of clo radical using velocity map ion imaging. *jcp*, 123:174303, 2005.

[5] Ian C. Lane, Wendy H. Howie, and Andrew J. Orr-Ewing. The uv absorption of clo part 2. *pccp*, 1:3087–3096, 1999.

[6] Hahkjoon Kim, Kristin C. Dooley, Gerrit C. Groenenboom, and Simon W. North. Vibrational state-dependent predissociation dynamics of clo ($a^2\pi_{3/2}$): Insight from correlated fine structure branching ratios. *pccp*, 8:2964–2971, 2006.

[7] Patrick W. McLoughlin, Chan Ryang Park, and John R. Wiesenfeld. High-resolution real time laser absorption spectroscopy of clo $a^2\pi$-$x^2\pi$. *jmolspec*, 162:307–326, 1993.

[8] S.A. Barton, J.A. Coxon, and U.K. Roychowdhury. Absolute absorption cross sections at high resolution in the $a^2\pi_i$ - $x^2\pi_i$ band system of clo. *canjp*, 62:473–486, 1983.

[9] G.W.M. Vissers, G.C. Groenenboom, and A. van der Avoird. Spectrum and vibrational predissociation of the hf dimer. ii. photodissociation cross sections and product state distributions. *jcp*, 119:286–292, 2003.

[10] NL Singh and DC Jain. The rydberg-klein-rees method of constructing the true potential energy curves of diatomic molecules. *Proc. Phys. Soc.*, 79:274, 1962.

[11] John Brown and Alan Carrington. *Rotational Spectroscopy of Diatomic Molecules*. Cambridge Molecular Science. Cambridge University Press, 2003.

[12] D.M. Brink and G.R. Satchler. *Angular Momentum*. Oxford University Press, 1993.

[13] Gerrit C Groenenboom and Daniel T. Colbert. Combining the discrete variable representation with the s-matrix kohn method for quantum reactive scattering. *jcp*, 99:9681–9696, 1993.

[14] H.-J. Werner and P. J. Knowles. *Molpro*. Complete system of *ab initio* programs for molecular electronic structure calculations, for more information see: www.molpro.net.

[15] Scilab 4.1.1. Open source platform for numerical computation, for more information see: www.scilab.org.